The Airborne Demonstrator for the Direct-Detection Doppler Wind Lidar ALADIN on ADM-Aeolus. Part I: Instrument Design and Comparison to Satellite Instrument

OLIVER REITEBUCH, CHRISTIAN LEMMERZ, ENGELBERT NAGEL, AND ULRIKE PAFFRATH

Deutsches Zentrum für Luft- und Raumfahrt, Institut für Physik der Atmosphäre, Oberpfaffenhofen, Germany

YANNIG DURAND AND MARTIN ENDEMANN

European Space Agency, Noordwijk, Netherlands

FREDERIC FABRE AND MARC CHALOUPY*

EADS Astrium, European Aeronautic Defense and Space Company, Toulouse, France

(Manuscript received 23 March 2009, in final form 29 June 2009)

ABSTRACT

The global observation of profiles of the atmospheric wind speed is the highest-priority unmet need for global numerical weather prediction. Satellite Doppler lidar is the most promising candidate to meet the requirements on global wind profile observations with high vertical resolution, precision, and accuracy. The European Space Agency (ESA) decided to implement a Doppler wind lidar mission called the Atmospheric Dynamics Mission Aeolus (ADM-Aeolus) to demonstrate the potential of the Doppler lidar technology and the expected impact on numerical weather forecasting. An airborne prototype of the instrument on ADM-Aeolus was developed to validate the instrument concept and retrieval algorithms with realistic atmospheric observations before the satellite launch. It is the first airborne direct-detection Doppler lidar for atmospheric observations, and it is operating at an ultraviolet wavelength of 355 nm. The optical design is described in detail, including the single-frequency pulsed laser and the two spectrometers to resolve the Doppler frequency shift from molecular Rayleigh and aerosol Mie backscatter. The airborne prototype is representative of the spaceborne instrument, and their specific differences are discussed.

1. Introduction

In 1999, the European Space Agency (ESA) decided to implement a Doppler wind lidar (DWL) mission called the Atmospheric Dynamics Mission Aeolus (ADM-Aeolus). The mission will provide profiles of one component of the horizontal wind vector from ground up to the lower stratosphere (20–30 km) with 0.5–2-km vertical resolution and a precision of 1–3 m s^{-1}, depending on altitude. A line-of-sight (LOS) wind profile will be obtained every 200 km with a horizontal averaging length of 50 km (ESA 1999, 2008; Stoffelen et al. 2005).

The ADM-Aeolus payload Atmospheric Laser Doppler Instrument (ALADIN) is based on a direct-detection Doppler wind lidar operating at 355 nm (Schillinger et al. 2003; ESA 2008). The receiver consists of two spectrometers to determine the Doppler shift from the spectrally broad Rayleigh molecular return and the spectrally narrow Mie return from aerosols and clouds. ALADIN will be the first wind lidar (Endemann et al. 2004; Morancais et al. 2004) and the first high-spectral-resolution lidar (HSRL) in space (Ansmann et al. 2007; Flamant et al. 2008).

A prelaunch campaign program for ADM-Aeolus was established taking into account the following:

- The satellite instrument will be tested and characterized on ground in a clean-room environment, but

* Current affiliation: European Patent Office, Munich, Germany.

Corresponding author address: Oliver Reitebuch, Deutsches Zentrum für Luft- und Raumfahrt, Institut für Physik der Atmosphäre, Oberpfaffenhofen, 82234 Wessling, Germany.
E-mail: oliver.reitebuch@dlr.de

DOI: 10.1175/2009JTECHA1309.1

without exposing it with atmospheric signals before launch (Endemann et al. 2008).
- Direct-detection Doppler wind lidars were operated in the past from the ground (e.g., McGill et al. 1997b; Delaval et al. 2000; Gentry et al. 2000; Yoe et al. 2003; Shen et al. 2008), but no direct-detection Doppler lidar was deployed on an airborne platform in a downward-looking geometry as from space: likewise for coherent Doppler lidars (Reitebuch et al. 2001; Weissmann et al. 2005).
- ALADIN combines new techniques that were not implemented in a wind lidar before, such as a novel combination of the molecular and aerosol spectrometers, the use of a Fizeau interferometer for the narrowband aerosol return, a sequential implementation of the double-edge Fabry–Perot for molecular return, and the use of two accumulation charge coupled devices (ACCDs) as detectors.

The development of an airborne instrument demonstrator was started by the European Aeronautic Defence and Space Company (EADS-Astrium) and Deutsches Zentrum für Luft- und Raumfahrt (DLR) in 2003, and it was called the ALADIN Airborne Demonstrator (A2D). The main objective of the airborne instrument demonstrator is the validation of the ALADIN instrument and performance models from ground and from an airborne platform (Reitebuch et al. 2004, 2008; Durand et al. 2005, 2006). Furthermore, atmospheric observations with an ALADIN-type instrument from various atmospheric scenes (e.g., clear air without clouds, different cloud types or aerosol loadings, surface returns) should be obtained to test, validate, and optimize the retrieval and related quality-control algorithms, as well as the calibration schemes for the space instruments (Reitebuch et al. 2006; Dabas et al. 2008; Flamant et al. 2008; Tan et al. 2008). An end-to-end instrument simulator including the retrieval algorithms was developed for the airborne demonstrator to assess the radiometric and wind measurement performance (Paffrath 2006). The simulator and the validation of the radiometric performance are described in Paffrath et al. (2009, hereafter Part II), whereas the measurement and modeling of the sea surface reflectance under different incidence angles at the wavelength of 355 nm with the A2D is studied by Li et al. (2010).

The ALADIN airborne demonstrator is the first airborne direct-detection Doppler lidar for long ranges and was deployed on an aircraft in October 2005 for the first time. True-airspeed vector measurements at short ranges of 50–150 m were performed already in 2004 by an airborne direct-detection Doppler lidar (Schmitt et al. 2007). The ongoing development of an airborne direct-detection Doppler lidar with a holographic scanning device is described by Gentry et al. (2008).

Section 2 gives an overview of the principle of direct-detection Doppler wind lidar and its various realizations. Section 3 describes the design of the airborne instrument demonstrator in detail, whereas section 4 discusses the representativeness of the airborne ALADIN instrument design with respect to the satellite instrument.

2. Principle of direct-detection Doppler wind lidar

DWL systems determine the LOS wind speed as a function of range by detecting the change in wavelength and frequency of the emitted laser pulse. The moving atmospheric particles (aerosol, cloud particles, and molecules) cause a frequency shift Δf in the backscatter signal of the emitted laser frequency f_0 because of the Doppler effect, which is proportional to the ratio of the wind velocity along the laser beam LOS v_{LOS} and the speed of light c of 2.998×10^8 m s^{-1} with $\Delta f = 2f_0 v_{LOS}/c$. An LOS wind velocity v_{LOS} of 1 m s^{-1} corresponds to a shift in frequency Δf of 5.635 MHz and wavelength shift $\Delta\lambda$ of 2.368 fm for the frequency f_0 of 844.7 THz and wavelength λ_0 of 354.9 nm used by the ALADIN instrument, respectively. The required accuracy in the measurement of the relative Doppler shift $\Delta f/f_0$ is on the order of 10^{-8} to achieve an accuracy of 1 m s^{-1}. Thus, a DWL requires spectrally narrow and frequency-stabilized laser sources; therefore, single longitudinal mode operation is mandatory, which is challenging to achieve for airborne lidars because of aircraft vibrations (cf section 3c).

On the one hand, the Doppler shift can be determined from the spectrally narrowband Mie backscatter return of aerosol or cloud particles, with the spectral width of the emitted laser pulse and slightly broadened by atmospheric turbulence. This results in typical line widths of a few m s^{-1} up to 10 m s^{-1} full width at half maximum (FWHM) for the narrowband Mie return independent from the chosen laser wavelength, which can be converted to the more usual line width in units of frequency by the earlier equation for Doppler shift. Coherent or heterodyne Doppler wind lidars usually operate at near-infrared wavelengths (1, 1.5–1.6, or 2 μm) by using solid-state or fiber lasers or operate at infrared wavelengths (10.6 μm) with CO_2 gas lasers. Coherent wind lidars spectrally resolve the narrowband aerosol and cloud return by optically beating the backscattered signal with light from a continuous-wave local oscillator laser. On the other hand, the Doppler shift can be determined from the spectrally broadband Rayleigh–Brillouin return of molecules, which is caused by the

thermal Brownian movement of the molecules modified by Brillouin scattering in the atmosphere (Tenti et al. 1974; Dabas et al. 2008). Typical line widths for the broadband Rayleigh return are in the range of 580–690 m s^{-1} FWHM for atmospheric temperatures of −60° to +30°C; thus, they are two orders of magnitude larger than the narrowband Mie return.

Direct-detection (also called incoherent) Doppler lidars operate usually at wavelengths provided by an Nd:YAG laser in the near infrared at 1.06 μm (fundamental), in the visible at 0.532 μm (second harmonic), or in the ultraviolet (UV) at 0.355 μm (third harmonic). They can be used to determine the wind speed from both the broadband Rayleigh and the narrowband Mie backscatter.

Measuring global atmospheric winds from space was initially proposed, and then its performance was simulated for the coherent detection at 10.6 μm using CO_2 lasers by Huffaker (1978) and Huffaker et al. (1984) and for the direct-detection technique using frequency-doubled Nd:YAG lasers at 532 nm by Abreu (1979). ADM-Aeolus, with the direct-detection Doppler lidar ALADIN, spectrally resolves both the Mie and Rayleigh backscatter by using two spectrometers to sense the wind velocity, both in regions with high aerosol loads and clouds and in regions with very low aerosol content in the upper troposphere or lower stratosphere up to 30 km, yielded toward giving the most impact to numerical weather prediction (Stoffelen et al. 2005; ESA 2008).

The principle of wind measurements with direct-detection Doppler lidar was first described and realized by Benedetti-Michelangeli et al. (1972) with a frequency-stabilized argon ion laser emitting at 488 nm and a spherical Fabry–Perot interferometer as spectral analyzer.[1] Direct-detection Doppler lidar use one or more narrowband filters and determine the Doppler frequency shift from the transmitted signal strength through this filter, which is called the edge technique (Korb et al. 1992, 1998; McKay 1998a; Flesia and Korb 1999), or from the radial angular distribution or spatial movement of the interference patterns (''fringes'') of an interferometer, which is called the fringe-imaging technique (McKay 1998b; McGill and Spinhirne 1998 for a comparative overview). Because of the difference in spectral width of the Mie and Rayleigh atmospheric signal by one to two orders of magnitude, the implementation of the interferometer must be optimized to either the Mie or Rayleigh spectral line width. Because the transmitted signals through the filters are the convolution of the filter transmission curves and the spectrum of the atmospheric backscattered signal, the spectral response has to be characterized for both the narrowband Mie and the broadband Rayleigh signal separately. In addition, a correction for atmospheric temperature and pressure has to be performed for Rayleigh wind retrievals (Dabas et al. 2008) because of the temperature-dependent broadening of the Rayleigh line, which is proportional to $\sqrt{T}$, modified by the pressure dependent Brillouin scattering (Tenti et al. 1974).

If the filter maximum is placed at the steepest slope of the atmospheric spectral line (''turning point'' or edge), then a Doppler frequency shift results in a maximum change in filter transmission. An increase in sensitivity and accuracy is achieved when two filters are symmetrically placed around the spectral line maximum in both edges of the spectrum. The double-edge technique was pioneered by Chanin et al. (1989) and Garnier and Chanin (1992) for stratospheric winds using the broadband molecular return with a laser wavelength of 532 nm and by Korb et al. (1992, 1998) and Gentry et al. (2000) for tropospheric winds using laser wavelengths of 1064 and 532 nm for the narrowband aerosol return and 355 nm for the molecular return.

The double-edge technique is widely used to determine the Doppler shift from Rayleigh return in the UV at 355 nm (Flesia et al. 2000; Gentry et al. 2000; Imaki and Kobayashi 2005; Sun et al. 2008), as implemented for ALADIN, or at visible wavelengths of 532 nm (Chanin et al. 1989; Garnier and Chanin 1992; Souprayen et al. 1999; Sun et al. 2008). Double-edge lidar systems for observing the narrowband aerosol return using 1064 nm were applied for lower tropospheric winds (Korb et al. 1997; Xia et al. 2007; Shen et al. 2008) and at 355 nm as a combined HSRL and DWL by Imaki and Kobayashi (2005). The fringe-imaging technique was applied by Abreu et al. (1992), Fischer et al. (1995), McGill et al. (1997a,b), Irgang et al. (2002), Dehring et al. (2003), and Schmitt et al. (2007). The ADM-Aeolus instrument ALADIN uses the double-edge technique for the molecular Rayleigh return and the fringe-imaging technique for the aerosol Mie return.

The single-edge technique can be realized by using iodine molecular absorption lines as narrowband filters for both molecular and aerosol backscatter at 532 nm (Liu et al. 1997, 2007; see comparative overview in She et al. 2007) and were recently applied to measure sea surface winds during the 2008 Olympic Games in Bejing, China (Liu et al. 2008). The iodine filter technique is also used for wind measurements up to 70 km (Fiedler et al.

[1] These first atmospheric wind lidar observations (the authors used the term ''optical radar'') were performed in 1971 at the European Space Research Institute (ESRIN) in Frascati, Italy. Today, ESRIN is part of ESA and will be responsible for the ADM-Aeolus mission after commissioning phase following the satellite launch scheduled for 2011.

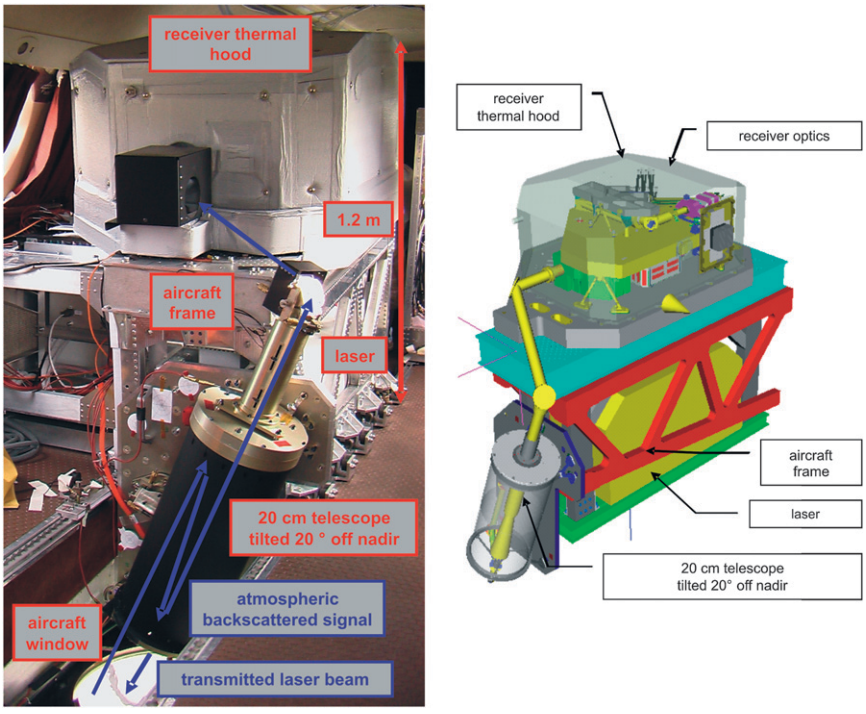

FIG. 1. (left) The A2D integrated in the DLR Falcon 20 aircraft during its initial test flights in October 2005 and (right) a sketch of the principal setup.

2008). Combined wind and temperature measurements up to 50 km with a Na double-edge magneto-optic filter were reported recently (Huang et al. 2009). The use of the Mach-Zehnder interferometers as spectral analyzers was proposed for the narrowband aerosol signal by Liu and Kobayashi (1996), proposed for the broadband molecular signal by Bruneau (2001), and demonstrated by Bruneau et al. (2004), whereas a fringe-imaging Michelson interferometer was proposed by Cezard et al. (2006).

3. Design and setup of the ALADIN airborne demonstrator

The airborne instrument version A2D of the satellite instrument ALADIN was developed by EADS-Astrium and DLR from 2003 to 2007. The core of the A2D is based on the ALADIN receiver and transmitter from the predevelopment program of ESA (Durand et al. 2005, 2006), and is therefore representative of the actual satellite instrument. The optical receiver of the A2D was space qualified with respect to its thermal vacuum and vibration environment during the predevelopment phase. Differences between the airborne and satellite instrument are discussed in section 4.

The first flights were performed in October 2005, and the development phase of the A2D was finished in April 2007, where it was demonstrated that the required frequency stability of the laser was achieved even with considerable aircraft vibrations. The A2D and the DLR coherent 2-μm wind lidar (Köpp et al. 2004; Weissmann et al. 2005) were both installed on the DLR Falcon 20 aircraft in November 2007, which is the first time that a coherent and a direct-detection Doppler wind lidar were operated simultaneously onboard an aircraft (Reitebuch et al. 2008).

a. *Airborne instrument design*

The A2D is a nonscanning lidar as the satellite instrument. Thus, only one LOS component of the three-dimensional wind vector is measured in contrast to most other direct-detection wind lidars, which are equipped with a scanning device. The LOS wind is measured perpendicular to the aircraft roll axis, with an off-nadir angle of 20°. The A2D is designed to be operated on the DLR Falcon 20 aircraft, a twin-engine jet with a pressurized cabin allowing a maximum payload of 1.1 ton, a flight altitude of up to 12 km, and range of up to 3700 km. The installation of the A2D inside the Falcon aircraft is shown in Fig. 1 with the telescope, the mechanical aircraft frame, and the thermal hood of the receiver system. The mechanical frame holding the telescope, receiver, and laser is mounted via vibration-damping shock mounts to the seat rails of the aircraft. The mechanical frame of the 10.6-μm heterodyne wind

infrared Doppler lidar (WIND; see Werner et al. 2001; Reitebuch et al. 2001), which has proven its aircraft vibration-damping behavior needed for coherent detection, was adapted to hold the A2D laser, optical receiver, and telescope.

The laser beam is directed toward the atmosphere via a window in the bottom fuselage of the aircraft cabin. The electronic units operating the A2D are installed in 19-in. aircraft racks and are controlled by two operators. The total volume of the system is 3 m^3, the weight is 550 kg, and the mean power consumption is 2.5 kW. Finite element simulations were performed to minimize the overall weight, providing high stiffness for the transmit and receive optical path, and to prove airworthiness.

The A2D can be operated from ground within a container using the same mechanical setup as in the aircraft with the telescope pointing toward the ground. Thus, an additional reflecting mirror is installed to point the beam toward the atmosphere up to 20° off-zenith angles.

b. Optical design overview

The narrowband single-frequency laser pulses at 354.89-nm vacuum wavelength are generated by an Nd:YAG laser. The circularly polarized laser pulses are transmitted via three reflecting mirrors through the aircraft window (or one reflecting mirror in case of ground operation) toward the atmosphere. The last reflecting mirror is placed on the telescope optical axis and thus a coaxial transmit–receive system is obtained. The backscattered photons from the atmosphere are collected by a 20-cm aperture Cassegrain telescope and directed to the optical receiver via an optical relay with two lenses and two mirrors. After passing the front optic with field and aperture stop, the light is directed toward the two spectrometers. The Rayleigh spectrometer uses the double-edge technique with a sequential Fabry–Perot interferometer, whereas the Mie spectrometer is based on a Fizeau interferometer. For both the Rayleigh and the Mie spectrometer, an ACCD detector is used, and the electronic signal is digitized after preamplification. The sequential implementation of the Fabry–Perot interferometer and the ACCD are patented by Astrium. The optical beam path with about 60 optical elements and the alignment sensitivities were studied in detail with an optical ray-tracing model. The principle layout of the A2D optical design is shown in Fig. 2. The main instrument parameters for the satellite ALADIN and the A2D are summarized in Table 1. The front optics and both spectrometers are integrated on both sides of an optical bench shown in Fig. 3. In the following subsections, the A2D laser transmitter, the telescope and front optics, the spectrometers, and the electronic detection chain are described in more detail.

c. The A2D laser transmitter

The A2D laser transmitter consists of a frequency-tripled, diode-pumped, pulsed Nd:YAG laser with an output energy of 55–65 mJ, a pulse repetition rate of 50 Hz, a pulse duration of 25 ns (FWHM), and a line width of 45 MHz (FWHM) at 354.89 nm. The optical design and performance of the A2D laser transmitter is described in detail in Schröder et al. (2007). The A2D laser uses an injection-seeded master oscillator power amplifier (MOPA) configuration, which is similar to single-frequency laser designs for airborne applications described by Hovis et al. (2008) and Wirth et al. (2009). The single-shot frequency performance is verified with a heterodyne method at 1064 nm, whereas the laser absolute wavelength is monitored with a commercial wavelength meter (HighFinesse WS Ultimate 10). The heterodyne method allows monitoring of the relative frequency stability of the pulsed laser output compared to the continuous-wave seed laser with an accuracy of better than 10 kHz for every single laser pulse. The wavelength meter allows measuring the laser absolute mean wavelength for 4–6 pulses with an accuracy of about 2 MHz (corresponding to a relative accuracy of 2×10^{-9}), thanks to its continuous calibration to a He–Ne laser line. During flights with the A2D in October 2005, it was not possible to operate the laser in a single-frequency and seeded mode because of aircraft vibrations. Compared to the design described by Schröder et al. (2007), the master oscillator unit was mechanically modified, and the active cavity control technique for the master oscillator was changed from pulse built-up time minimization to ramp fire. A shot-to-shot frequency variation of less than 0.6 MHz at 1064 nm (corresponding to 1.8 MHz at 355 nm) was obtained during flights in April 2007, even with considerable aircraft vibrations (Witschas 2007). To the authors knowledge a comparable low-frequency jitter for pulsed, high-energy lasers, which corresponds to a relative frequency stability of 2×10^{-9}, was not demonstrated before for airborne lasers and is not even achieved by most single-frequency lasers operated without vibrations in a laboratory environment.

The laser transmitter is tunable in frequency over a spectral range of ±5.5 GHz (UV) to calibrate the spectral response of the Rayleigh spectrometer. This is achieved by tuning the seed laser frequency by means of temperature tuning of the seed-laser crystal.

The laser beam profile and divergence was characterized by using the converging lens method according to ISO (1999) with an accuracy of ±10%. Values of 1.9 (1.7) were obtained for the M^2 value for the major (minor) axis at the laser UV output in 2007, resulting in a $\pm 3\sigma$ beam divergence of 190 (210) μrad for beam

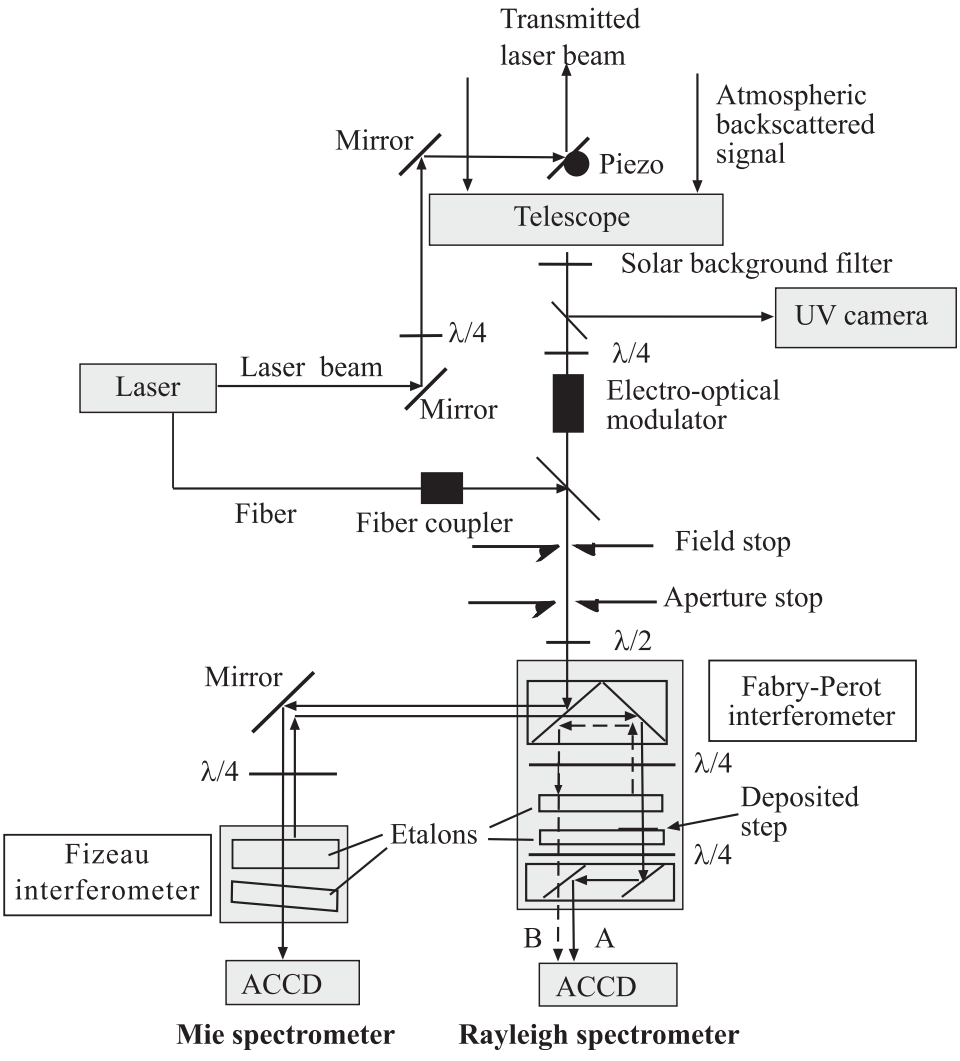

FIG. 2. Schematic optical layout of the A2D.

diameters of 6.5 (5.6) mm. Because the receiver field of view (FOV) is only 100 μrad, the higher laser beam divergence results in a significant signal loss (see Part II). After increasing the beam diameter and optimization of the alignment through the power amplifier and higher-harmonic crystals, an almost Gaussian beam profile with M^2 of 1.2 and a divergence of below 90 μrad ($\pm 3\sigma$) was obtained.

The seed- and power-laser diodes are temperature stabilized with a water cooling system to 16° ± 0.1°C. The heat of this water cooling system is removed to the outside of the aircraft by a two-stage liquid cooling system.

d. Telescope and front optics

The Cassegrain telescope is composed of a 200-mm concave, aspheric primary mirror and a 75-mm convex, spherical secondary mirror with a telescope focal length of 1.5 m, resulting in an f-number of f/7.5. The transmit path mirror is mounted on the optical axis of the telescope at the backside of the secondary mirror. A pair of lenses after the secondary mirror acts as an ocular, turning the telescope into a focal system with a collimated output beam and a magnification of 21.4. The light is directed toward the optical receiver via a free optical path relay consisting of two mirrors and two lenses. In contrast, most other direct-detection lidar systems (e.g., Korb et al. 1997; Souprayen et al. 1999; Gentry et al. 2000; Irgang et al. 2002; Imaki and Kobayashi 2005; Liu et al. 2007; Xia et al. 2007) use fiber coupling between telescope and spectrometers. The fiber coupling eases optomechanical integration and stability and generates uniform illumination of the spectrometers by spatial mode scrambling of the atmospheric signal (Grund and

TABLE 1. Specifications of the satellite ALADIN and measured performance of the A2D.

	Satellite ALADIN	A2D
Platform	Satellite	Container or DLR Falcon aircraft
Alt	408 km	Ground or 8–12 km flight alt
LOS pointing	37.6° off nadir	0°, 15–20° off zenith (ground) 20° off nadir (aircraft)
Min vertical resolution	250 m for 2.1 μs at 37.6° off nadir	315 m for 2.1 μs at 0° zenith
Laser transmitter	Nd:YAG, frequency-tripled, diode-pumped	
Wavelength	354.9 nm	354.89 nm
Operation	Burst mode	Continuous
Pulse repetition rate	100 Hz	50 Hz
Energy per pulse	120 mJ	55–65 mJ
Laser line width	<50 MHz (FWHM)	45 MHz (FWHM)
Pulse-to-pulse frequency stability in the UV	<4 MHz rms over 7 s	<1.8 MHz rms over 14 s 4.5 MHz peak to peak
Laser divergence	12 μrad	80–90 μrad for $\pm 3\sigma$, 99.7% (190–210 μrad until November 2007)
Laser beam diameter	1.5 m	16 mm (99.7%) (8 mm until November 2007, 99.7%)
Laser output polarization	Circular left	
Laser internal reference path	Free path with aberration generator	Multi mode fiber with polarizer
Telescope and receiver	Transceiver telescope; same transmit and receive path	Receiver Cassegrain telescope Separate transmit and receive paths
Telescope diameter	1.5 m	0.2 m
Receiver FOV	19 μrad	100 μrad
Background blocking filter bandwidth FWHM	1 nm	2.6 nm
Mie spectrometer	Fringe-imaging Fizeau interferometer, 16 spectral channels	
Rayleigh spectrometer	Double-edge Fabry–Perot interferometer, 2 filters, sequential	
Detector	Accumulation CCD, quantum efficiency 0.85	

Eloranta 1991). Because the satellite instrument contains no fiber coupling from the telescope to the receiver, it was not implemented for the A2D. Significant transmission losses up to 50% in the case of the ALADIN instrument would be introduced by the use of nonpolarizating maintaining, multimode fibers because of the polarization-dependent receiver and spectrometer optics.

Polarizing optical elements turn the input circular polarized light from the atmosphere into linear polarized light. Depolarization in the atmosphere resulting from aspherical particles (e.g., ice particles within cirrus clouds or desert dust aerosol) will result in noncircular polarized light and will be reflected inside the front optics. Thus, depolarization within the atmosphere or the optics will result in a corresponding signal loss at the spectrometers.

Two filters for blocking visible and infrared light and a 2.6-nm FWHM interference filter centered at 355 nm are used to block solar background light. A circular diaphragm of 200 μm acts as a field stop within the front optics and limits the FOV of the telescope to 100 μrad at full angle. An aperture stop limits the beam diameter at the entrance plane of the spectrometers to 20 mm with a resulting divergence of 1 mrad (full angle), conserving the systems etendue (product of aperture and divergence).

To monitor the frequency of the transmitted laser pulse and to perform calibrations of the frequency-dependent transmission of the spectrometers, a small fraction of the UV light inside the laser is directed toward an integrating sphere and coupled via a multimode fiber (200-μm diameter, 4-m length) into the receiver front optics, allowing adjustable signal levels by a variable fiber attenuator. The fiber diameter and collimating optics are designed so that the field and aperture stops are fully illuminated by the laser internal reference. An electro-optical modulator (Lasermetrics T1042) is used to block the atmospheric path after laser-pulse emission by a variable time of usually 3 μs, corresponding to 450 m, to avoid disturbances of the laser internal reference measurement by atmospheric signal and to avoid saturation of the detectors at short ranges.

To control the angular coalignment between the transmit and receive path (optical axis of telescope, field stop, and spectrometers) a UV-sensitive charge-coupled device (CCD) camera (Sony XC-EU50CE) monitors

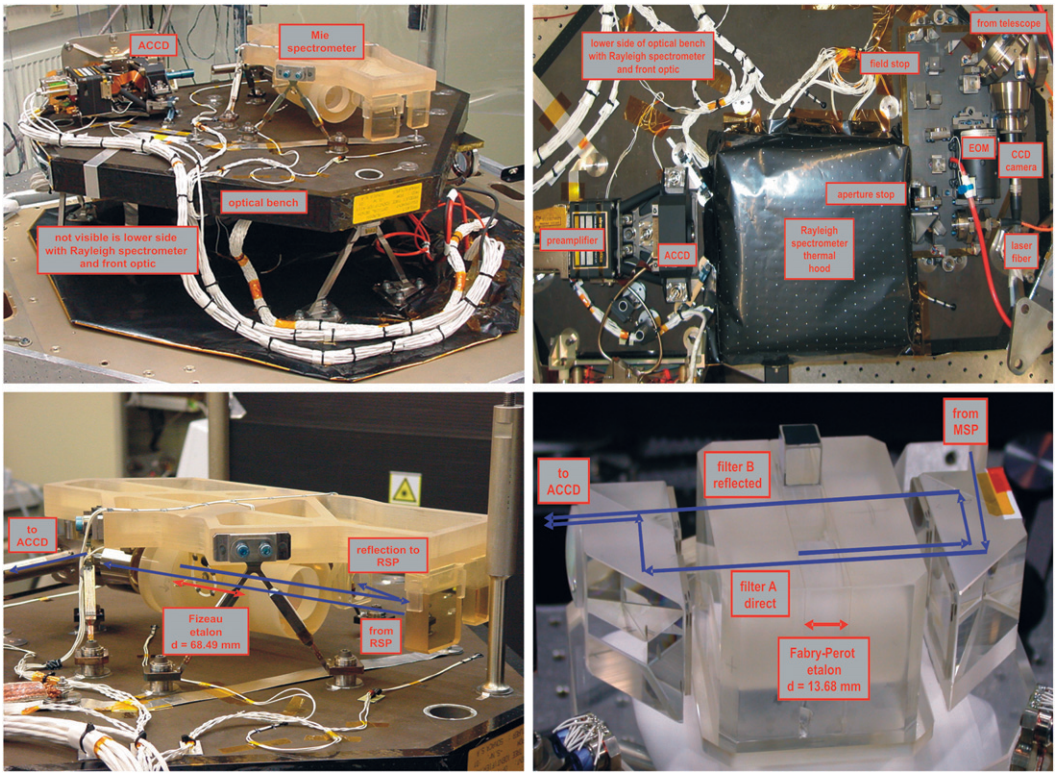

FIG. 3. (top left) A2D receiver optical bench with Mie spectrometer MSP and ACCD detector and (top right) lower side with Rayleigh spectrometer RSP thermal hood and front optics including electro-optical modulator EOM; (bottom left) Mie spectrometer with Fizeau interferometer etalon and additional optics; and (bottom right) Rayleigh spectrometer with Fabry–Perot interferometer etalon and additional optics with blue arrows indicating the optical beam path.

the integrated backscatter from the atmosphere. The spot position on the CCD camera corresponds to different incidence angles of the backscattered signal with respect to the receive path optical axis. The deviation of the center of gravity of the backscattered atmospheric signal on the CCD camera from a reference position, which corresponds to the center of the field stop, is used to automatically steer the direction of the transmit path mirror by three piezoelectric actuators. This coalignment loop centers the integrated atmospheric backscatter from the laser onto the receiver FOV and compensates for thermoelastic and laser pointing drifts. The angular stability of the active coalignment loop depends on the measured laser beam motion in the atmosphere, which is mainly caused by atmospheric turbulence and partly caused by laser beam pointing jitter. For ground operation, the measured angular stability is between ± 1 to ± 5 μrad and about ± 5 μrad for airborne operation, compared to the total atmospheric FOV of 100 μrad. The active coalignment is specifically needed for the A2D and not for the satellite instrument (cf. section 4).

e. Mie and Rayleigh spectrometer

A Fizeau interferometer is used for measuring the frequency of the narrowband Mie backscatter from aerosol and cloud particles, whereas a Fabry–Perot interferometer is used to measure the broadband Rayleigh return from molecules. The fringe-imaging technique with Fizeau interferometers was developed for the ALADIN instrument (ESA 1999) and theoretically discussed by McKay (2002). The ALADIN Fizeau interferometer was the only one used for wind lidar applications, until an almost identical concept was realized recently (Bu et al. 2008). In contrast, the double-edge technique with Fabry–Perot interferometers is widely used in direct-detection Doppler lidars, but not in a sequential implementation as for ALADIN. Both the spectrometer etalons are evacuated between the reflecting plates and are manufactured by optically contacting the plates to a fused silica spacer for the Rayleigh and a spacer made of Zerodur for the Mie spectrometer. Photos of both spectrometers and the optical beam path are shown in Fig. 3 (bottom), and

TABLE 2. Specifications of the Mie spectrometer, Rayleigh spectrometer, and detector for the satellite and airborne ALADIN instrument.

Mie spectrometer	Fringe-imaging Fizeau interferometer
Spectrometer material	Zerodur
Spectral channels	16
Etalon plate spacing	68.49 mm, vacuum gap
Etalon wedge angle	4.77 μrad
Fizeau FSR	0.92 pm/2.2 GHz
Fizeau USR	0.69 pm/1.6 GHz
Fizeau FWHM	0.0575 pm/0.135 GHz, not including broadening through accumulation of signal
Effective finesse	16
Etalon aperture	36 mm
Input divergence	0.555 mrad full angle
Rayleigh spectrometer	Double-edge Fabry–Perot interferometer
Spectrometer material	Fused Silica
No. of filters	2 in sequential implementation
Etalon plate spacing	13.68 mm, vacuum gap
Frequency tuning	Temperature
Fabry–Perot FSR	4.6 pm/10.95 GHz
Fabry–Perot FWHM	0.75 pm/1.78 GHz
Effective finesse	6.6
Rayleigh filter spacing between A and B	2.3 pm/5.5 GHz (satellite ALADIN) 2.6 pm/6.2 GHz and 2.0 pm/4.75 GHz (A2D)
Etalon aperture	20 mm
Input divergence	1 mrad full angle
Detector	ACCD
Quantum efficiency	0.85 electrons per photon
No. of pixels	16×16 in image zone corresponding to 16 pixels per range gate 25×32 in memory zone corresponding to 25 range gates
Temporal resolution	2.1 μs corresponding to 315 m range gates
Total noise including readout noise	5–7 electrons per pixel
Analog–digital converter	16 bit

Table 2 summarizes the specifications of the spectrometers and detection chain.

First, the light is reflected at a polarizing beam splitter toward the Mie spectrometer and increased in diameter by a beam expander to 36 mm to reduce the divergence to 555 μrad (not shown in Fig. 2). The Mie spectrometer is composed of a Fizeau interferometer acting as a narrowband filter with an FWHM of 57.5 fm. It is composed of two reflecting plates at a distance of 68.49 mm and a wedge angle of 4.77 μrad. It produces linear interference patterns (fringes), which are imaged onto the ACCD on different pixel columns. Because of the wedge angle, different wavelengths interfere on different lateral positions along the wedge. The width of the Fizeau fringe gets slightly broadened after accumulation of 700 laser return pulses on the ACCD to an FWHM of 59 fm, which is caused by the laser frequency jitter during the accumulation periods of 7 and 14 s (for satellite ALADIN and A2D, respectively). The fringe produced by the central part of the backscattered atmospheric spectrum is used, which is composed of the narrowband aerosol return and 5%–10% of the broadband solar background and molecular spectrum. A Doppler wavelength shift results in a shift of the fringe position on the ACCD detector. From the Fizeau interferometer free spectral range (FSR) of 0.92 pm, only a part of 0.69 pm is imaged onto the 16 pixels of the ACCD, which is called useful spectral range (USR) and corresponds to a LOS wind measurement range of ± 145 m s^{-1}.

The reflected part of the signal spectrum from the Mie spectrometer is directed toward the Rayleigh spectrometer on the same beam path and linearly polarized in such a direction that the beam is now transmitted through the polarizing beam splitter. The Rayleigh spectrometer is based on the double-edge technique, where two spectral filters are placed at the steepest slope of the broadband Rayleigh spectral line, symmetrically around the transmitted wavelength. The spectral filters are realized by two Fabry–Perot interferometers, with an etalon surface distance of 13.68 mm for one filter and a reduced distance for the other filter. This is achieved by a deposited step of 88.7 nm within one etalon (Fig. 2), which corresponds to one-quarter of the laser wavelength. The two spectral filters are illuminated sequentially by using the reflection from one spectral filter to feed the other, which is a novel implementation of the double-edge technique. The Fabry–Perot interferometers are realized with an FSR of 4.6 pm and an FWHM of 0.75 pm for both filters. Ideally, one filter should be symmetrically placed in the middle of the FSR of the other filter, thus resulting in a spacing of both filter maxima of FSR/2 = 2.3 pm. Because the A2D is operated in ambient pressure and not in vacuum as in the satellite instrument, the pressure induces an additional mechanical forcing on the etalon plates, which results in an unsymmetrical spacing of both filters with 2.6 and 2.0 pm. An example of the measured filter transmission of both Rayleigh filters is shown in Fig. 4. Both the FSR and the spacing of the two filters are common in most double-edge Fabry–Perot interferometers operating at 355 nm as a result of optimizing the instrument performance (McKay 1998a; Flesia and Korb 1999; Gentry et al. 2000).

The Fabry–Perot interferometer is used a spectral filter with an FWHM of 0.75 pm and is illuminated with an almost collimated beam of 1 mrad full divergence. Thus, only the central 0th-order maximum of the interference

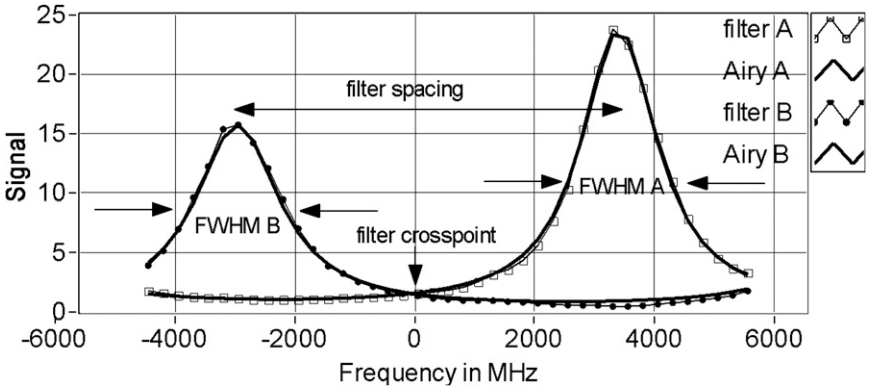

FIG. 4. Measured Rayleigh spectrometer signal in 10^4 analog–digital converter counts vs frequency in megahertz for direct path (filter A), reflected path (filter B), and fitted Airy function for each filter; filter cross point indicates frequency where wind measurements are performed, and filter spacing indicates frequency distance of both filter maxima.

pattern of the Fabry–Perot is imaged onto the ACCD detector, not a circular fringe pattern. Both filter transmission fringes are imaged on the same ACCD by a single lens, resulting in two separated circular spots on the ACCD.

Within the ALADIN instrument, the reflection on the Mie spectrometer is used as input for the Rayleigh spectrometer to utilize the reflected photons, which is conceptually similar to the system described by Irgang et al. (2002). The sequential implementation of the double-edge technique is a novel approach to gain higher radiometric efficiency for the Rayleigh spectrometer, which was not realized in other double-edge systems before. It results in different maximum transmissions for both filters, compared to a parallel implementation of the double-edge technique with equal filter transmission. Thus, the assumption of equal filter transmission maxima made for the optimization of the filter spacing to obtain equal sensitivity for broadband molecular and narrowband aerosol signal (Garnier and Chanin 1992; Korb et al. 1998; McKay 1998a; Flesia and Korb 1999) is not longer valid. The sensitivity to molecular return is about one-third higher than for aerosol return for the A2D Rayleigh spectrometer. A correction on the retrieved winds from the Rayleigh spectrometer in the case of high aerosol signals in the atmospheric boundary layer or from clouds can be applied by using the signal obtained from the Mie spectrometer (Dabas et al. 2008). In any case, the wind speed can be determined from the Mie spectrometer signal directly during high Mie backscatter conditions.

f. ACCD detectors

Two identical ACCDs are used as detectors for both the Mie and the Rayleigh spectrometer. CCD detectors with a large number of pixels of several 100×100 were used for wind lidar systems before (Irgang et al. 2002; Nardell et al. 2002; Dehring et al. 2003; Schmitt et al. 2007). The accumulation CCD of ALADIN uses only a small number of 16×16 pixels, each with a size of 27^2 μm^2, in the part of the ACCD where the spectrometer output is imaged. The ACCD is thinned and back-side illuminated for optimized operation in the UV to yield high quantum efficiency of 85%. It is cooled to -30°C to ensure a low electronic noise level. The ACCD allows the electronic charges from several atmospheric returns to be accumulated directly on the CCD within a second part, called the memory zone. This on-chip accumulation, which was implemented differently than the design described by Irgang et al. (2002), allows reading out the electronic charges with low readout noise.

The linear fringe of the Mie spectrometer is vertically imaged on the ACCD, and the electronic charges of all 16 rows are binned together to one row for each range gate of each laser pulse (Fig. 5). This results in 16 spectral channels for the Mie spectrometer, each corresponding to about 100 MHz or 17.7 m s^{-1}. The two spots from the Rayleigh spectrometer are both imaged on the same ACCD, centered on the right and left half of the ACCD. The center of both spots is separated by 8 pixels, and the electronic charges of all 16 rows are binned together to one row. The signal of each Rayleigh filter is then contained in 8 pixels, which are summed up after digitization in the retrieval algorithms.

The charges of the ACCD image zone are binned together for each range gate of each laser pulse and transferred to the memory zone of the ACCD. The charges of the memory zone are read out with low frequency to minimize readout noise after accumulating a number of settable laser pulses. The minimum number of accumulated atmospheric signal returns should be 20,

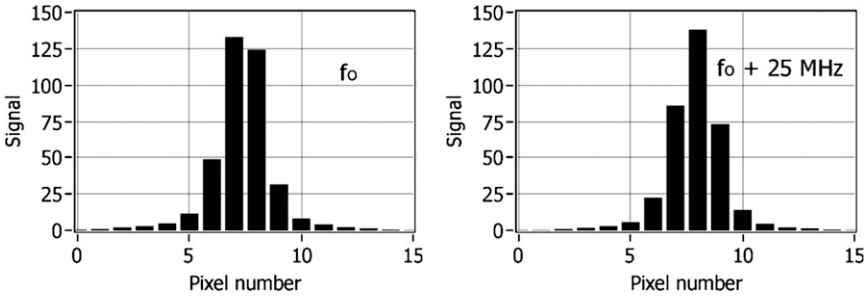

FIG. 5. Measured Mie spectrometer signal in 10^4 analog–digital converter counts from laser internal reference vs pixel number with frequencies of (left) f_0 and (right) f_0 + 25 MHz, corresponding to an LOS velocity of 4.4 m s^{-1}; one pixel corresponds to a frequency difference of 100 MHz and velocity difference of 17.7 m s^{-1}.

to limit the number of lost pulses to 10%, because a time of two laser-pulse acquisitions is needed for read-out. Because the memory zone contains 25 rows, a maximum number of 25 range gates can be acquired with the ACCD. The background light and the laser internal reference signal for the A2D are acquired in one range gate each. The transfer time from the image to the memory zone of the ACCD limits the minimum temporal resolution of one range gate to 2.1 μs, which corresponds to a range resolution of 315 m. The timing sequences of both ACCDs are programmable, giving flexibility in range gate resolution within one profile for both the Mie and Rayleigh return independently and also for the number of accumulated shots on the ACCD.

The photons at the input of the ACCD are converted to electrons with a quantum efficiency of 85% and a total noise of about 5–7 electrons per pixel, thus allowing quasi-photon counting. Detectors used for DWL operating in the UV as photomultiplier tubes usually provide a much smaller quantum efficiency of about 25% (Imaki and Kobayashi 2005; Gentry et al. 2000, 2008). After preamplification, the charges are digitized within 16 bit. In addition to the range-gated mode, the ACCD can be used in an imaging mode, where raw images of 16 × 16 pixels are acquired without any on-chip accumulation. This mode is mainly used for alignment and verification purposes.

g. *Thermal design and spectrometer thermal tuning*

The A2D receiver is enclosed in a thermal hood (Fig. 1), which is temperature stabilized better than 20–40 mK by utilizing five Peltier thermoelectric elements for cooling and heating. A sixth Peltier element is used for cooling both ACCD detectors to −30°C. The Rayleigh spectrometer is additionally enclosed inside the receiver (see Fig. 3, top right) and heated to achieve a temperature stability of ±10 mK. The Rayleigh spectrometer is made of Silica with a thermal expansion coefficient of 5.5×10^{-7} K^{-1}, resulting in a frequency change of 465 MHz K^{-1}. In contrast to that, the Mie spectrometer is made of Zerodur, which provides a 10–20 times lower thermal expansion coefficient. To center the Mie spectrometer USR onto the filter crossing point of the Rayleigh spectrometer, the operating temperature of the Rayleigh spectrometer is adapted. For measuring the frequency-dependent Rayleigh and Mie filters transmission, both the Rayleigh and the Mie spectrometer are kept at constant temperatures and the emitted laser frequency is changed in discrete frequency steps of usually 250 MHz over one full FSR of 11 GHz of the Rayleigh spectrometer (Fig. 4).

The wind measurements are performed at a laser frequency at the filter crossing point of the Rayleigh spectrometer and the center of the Mie spectrometer USR. The centering of the laser frequency to the Mie spectrometer USR is achieved by tuning the laser frequency until the signal on pixels 7 and 8 of the ACCD have about equal intensity (Fig. 5, left). The filter transmission and the resulting response curve for wind retrievals is similarly characterized by keeping the spectrometers at a constant temperature and tuning the laser frequency in discrete steps of usually 25 MHz over the wind measurement range of 1.0 GHz.

The characterization of the transmission of the spectrometers by varying the laser frequency at a constant spectrometer temperature differs from other approaches where the laser frequency is kept constant and the spectrometer etalon distance is varied with temperature, pressure, or piezoelectrical transducers (Garnier and Chanin 1992; Gentry et al. 2000; Xia et al. 2007).

4. Discussion of airborne and satellite instrument design

Because the A2D was developed to validate the satellite instrument principle and to derive conclusions on the

satellite instrument alignment, calibration, testing, and especially the retrieval algorithms, it was important to design the A2D as similarly as possible to the satellite instrument. A predevelopment program for the satellite ALADIN instrument receiver and laser transmitter was initiated by ESA, resulting in a prototype for the satellite receiver and a breadboard version of the laser transmitter (Durand et al. 2005, 2006). The ACCD, the detection electronic of the A2D, and in particular the receiver spectrometers design and implementation are almost identical to the satellite flight model. The laser transmitter principle with a injection-seeded, frequency-tripled Nd:YAG in MOPA configuration is similar for the satellite and airborne version, although the actual implementation is different. A detailed description of the satellite instrument design, specification, and implementation is found in ESA (2008, 45–75), complemented by an end-to-end performance simulation of the satellite instrument (Leike et al. 2001; Marseille and Stoffelen 2003).

A comparative overview of the airborne and satellite instrument parameters is provided in Table 1. Main differences of the A2D to the satellite instrument are the telescope, the transmit and receive optics, and the laser transmitter implementation. A 0.2-m Cassegrain telescope with an f-number of f/7.5 is used for the A2D and a coaxial, separate laser transmit path. A 1.5-m telescope with an f-number of f/0.9 in transceiver configuration is implemented for the satellite, where the same telescope is used for the transmit and receive path, resulting in a laser beam diameter of 1.5 m and a divergence of 12 μrad at the telescope output. The satellite instrument FOV is limited by the field stop to 19 μrad, compared to 100 μrad for the A2D. The transceiver telescope at the satellite allows a very small FOV without the need of active coalignment, which is necessary for the A2D. Because of the transceiver telescope configuration for the satellite, a mechanism is needed to optically block the receiver spectrometers during laser-pulse emission. In contrast, the airborne front optics include an electro-optical modulator for suppression of the near-field signal and a CCD camera for active coalignment of transmit–receive path, which is not needed for the satellite instrument. The coalignment performance strongly influences the incidence angle on both spectrometers and thus the retrieved Doppler frequency shift for the A2D. Because of the random variation of the coalignment (cf. section 3d) the wind random error for the A2D is above the level expected for shot-noise limited detection. To achieve this random error limit, it is planned to correct the retrieved wind values by a parameter characterizing the incidence angles on the spectrometers derived from the output of the UV camera inside the airborne front optics.

The airborne version uses a fiber coupling unit for the internal reference signal, whereas the satellite version uses free path propagation. For the satellite instrument, the laser internal reference signal is read out for every single laser pulse, because the time between emission and acquisition is sufficiently long, with about 3 ms. For the airborne instrument, the laser internal reference signal is accumulated on the ACCD as for the atmospheric range gates. The time between emission and first useful atmospheric range gate of 3 μs would be not sufficient to read out the ACCD for every single laser pulse.

Both Mie and Rayleigh spectrometers, the ACCD detectors, preamplifier, and detection unit are almost identical between airborne and satellite versions, except for some minor details in implementation resulting from different operation environments (vacuum versus aircraft cabin or ground pressure) and optimization of the flight-model instrument compared to the predevelopment model. The vacuum versus pressurized operation results in an important difference in the Rayleigh filter frequency spacing of 2.3 pm for vacuum compared to 2.6 pm, which was measured during ambient pressure. This results in different response slopes used for the wind retrievals.

The satellite laser emits laser pulses with an energy of 120 mJ at 354.9 nm and a pulse repetition rate of 100 Hz, and it operates in burst-mode, where the laser power amplifier diodes are switched off for 15 s, followed by a warm-up period of 6 s, and then operate during wind measurements for 7 s (Cosentino et al. 2004; ESA 2008). The A2D laser emits pulses with 60 mJ at 354.89 nm at a repetition rate of 50 Hz continuously. The principle of burst-mode operation is obtained for the A2D data acquisition, because a total of 700 laser pulses is acquired by the detection unit during 14 s, followed by a temporal gap of 4 s for the A2D resulting from data read out and transfer.

The range-corrected energy aperture product is more than 20 times larger for the A2D than for the satellite instrument for an altitude of 10 km and off-nadir angles. The different range-dependent signal dynamics are discussed in Part II. Different off-nadir angles of 37.6° (satellite), 20° (airborne), and 15°–20° (ground) result in different vertical range gate resolutions of 250 (satellite), 296 (airborne) and 304 m (ground, 15° zenith) for the same minimum temporal resolution of 2.1 μs of the ACCD.

In the case of airborne and ground-based operation, the atmospheric region of interest is close to the lidar while it is at large ranges for satellite lidars (e.g., 500 km for ADM-Aeolus on a 408 km orbit with 37.6° off nadir angle). Thus, any effect in the near field of the lidar within the first few kilometers (e.g., telescope overlap or range dependency of spectrometer illumination) is not present for the satellite system. On the other hand, effects of the

satellite orbital movement with respect to the earth's surface have to be compensated (e.g., latitude-dependent earth rotation with a maximum at the equator of 464 m s^{-1} or satellite rotations around its roll axis during laser-pulse travel time).

5. Summary and conclusions

The design of the airborne prototype of the Doppler wind lidar instrument on ADM-Aeolus is described. The single-frequency pulsed transmitter is based on a frequency-tripled Nd:YAG and achieves 60 mJ at 50 Hz with a frequency stability for every single laser pulse of better than 2 MHz, even under aircraft vibrations. To the authors' knowledge, a comparable low-frequency jitter for pulsed, high-energy lasers, which corresponds to a relative frequency stability of 2×10^{-9}, was not demonstrated before for airborne lasers.

The Doppler frequency shift from molecular Rayleigh backscatter is spectrally resolved by the double-edge method using a Fabry–Perot interferometer in a new sequential implementation for both filters. A Fizeau interferometer, which was not used before for atmospheric wind measurements, senses the Doppler shift from the narrowband aerosol Mie return. An ACCD detector with on-chip accumulation of the atmospheric signal from several laser pulses achieves photon-counting capabilities with high quantum efficiency of 85%.

The instrument optical throughput and thus radiometric performance was validated with observations compared to end-to-end simulations, which is described in Part II. Wind retrieval algorithms for the Rayleigh and Mie spectrometer output were developed and compared to ground-based observations from radiosondes and radar wind profilers. A detailed description of the instrument calibration and the wind retrieval algorithms and an examination of random and systematic wind errors will be given in a forthcoming paper. The high similarities of the airborne demonstrator for ALADIN and the satellite instrument allow validation and optimization of the wind retrieval algorithms and calibration of the instrument with realistic atmospheric signals before launch of the satellite.

Acknowledgments. The development of the ALADIN airborne demonstrator (A2D) was funded by ESA and DLR and performed by a team at DLR and EADS-Astrium (France, Germany), with contributions by E. Chinal, C. Hoeltzel, P. Mahnke, R. Treichel, T. Schröder, and C. Wührer. The review of the development activities by M. Alpers, A. Dabas, P. Flamant, D. Huber, H. Nett, O. LeRille, R. Meynart, A. Stoffelen, A. Straume, and M. Vaughan are highly acknowledged.

REFERENCES

Abreu, V. J., 1979: Wind measurements from an orbital platform using a lidar system with incoherent detection: An analysis. *Appl. Opt.,* **18,** 2992–2997.

——, J. E. Barnes, and P. B. Hayes, 1992: Observation of winds with an incoherent lidar detector. *Appl. Opt.,* **31,** 4509–4514.

Ansmann, A., U. Wandinger, O. Le Rille, D. Lajas, and A. G. Straume, 2007: Particle backscatter and extinction profiling with the spaceborne high-spectral-resolution Doppler lidar ALADIN: Methodology and simulations. *Appl. Opt.,* **46,** 6606–6622.

Benedetti-Michelangeli, G., F. Congeduti, and G. Fiocco, 1972: Measurement of aerosol motion and wind velocity in the lower troposhere by Doppler optical radar. *J. Atmos. Sci.,* **29,** 906–910.

Bruneau, D., 2001: Mach-Zehnder interferometer as a spectral analyzer for molecular Doppler wind lidar. *Appl. Opt.,* **38,** 391–399.

——, A. Garnier, A. Hertzog, and J. Porteneuve, 2004: Wind-velocity lidar measurements by use of a Mach-Zehnder interferometer, comparison with a Fabry-Perot interferometer. *Appl. Opt.,* **38,** 173–182.

Bu, L., K. Shan, X. Huang, J. Liu, J. Zhou, and W. Chen, 2008: Direct-detection wind lidar system based on Fizeau interferometer. *Proc. 24th Int. Laser Radar Conf.,* Boulder, CO, International Radiation Commission, 64–67.

Cezard, N., A. Dolfi-Bouteyre, J. P. Huignard, and P. Flamant, 2006: A 355-nm Rayleigh Mie lidar using two Michelson interferometers as spectral analyzers for multi-purpose near-field measurements. *Proc. 23rd Int. Laser Radar Conf.,* Nara, Japan, International Radiation Commission, 31–34.

Chanin, M. L., A. Garnier, A. Hauchecorne, and J. Porteneuve, 1989: A Doppler lidar for measuring winds in the middle atmosphere. *Geophys. Res. Lett.,* **16,** 1273–1276.

Cosentino, A., and Coauthors, 2004: All-solid-state laser transmitter for space based lidar applications. *Proc. 22nd Int. Laser Radar Conf.,* Matera, Italy, International Radiation Commission, 61–64.

Dabas, A., M. L. Denneulin, P. Flamant, C. Loth, A. Garnier, and A. Dolfi-Bouteyre, 2008: Correcting winds measured with a Rayleigh Doppler lidar from pressure and temperature effects. *Tellus,* **60A,** 206–215.

Dehring, M. T., C. A. Nardell, J. C. Pavlich, P. B. Hays, and I. Dors, 2003: Performance and comparison of 532-nm and 355-nm groundwinds lidars. *Lidar Remote Sensing for Industry and Environment Monitoring III,* T. Itabe and Z. Liu, Eds., International Society for Optical Engineering (SPIE Proceedings, Vol. 4893), 337–347.

Delaval, A., P. H. Flamant, M. Aupierre, P. Delville, and C. Loth, 2000: Intercomparison of wind profiling instruments during the VALID field campaign. *Proc. 20th Int. Laser Radar Conf.,* Vichy, France, International Radiation Commission, 101–104.

Durand, Y., R. Meynart, M. Endemann, E. Chinal, D. Morancais, T. Schröder, and O. Reitebuch, 2005: Manufacturing of an airborne demonstrator of ALADIN: The direct detection Doppler wind lidar for ADM-Aeolus. *Lidar Technologies, Techniques, and Measurements for Atmospheric Remote Sensing,* U. N. Singh, Ed., International Society for Optical Engineering (SPIE Proceedings, Vol. 5984), doi:10.1117/12.627789.

——, E. Chinal, M. Endemann, R. Meynart, O. Reitebuch, and R. Treichel, 2006: ALADIN Airborne Demonstrator: a Doppler Wind Lidar to prepare ESA's Aeolus Explorer Mission. *Earth Observing Systems XI,* J. J. Butler, Ed., International

Society for Optical Engineering (SPIE Proceedings, Vol. 6296), doi:10.1117/12.680958.

Endemann, M., P. Dubock, P. Ingmann, R. Wimmer, D. Morancais, and D. Demuth, 2004: The ADM-Aeolus mission—The first wind-lidar in space. *Proc. 22nd Int. Laser Radar Conf.,* Matera, Italy, International Radiation Commission, 953–956.

——, A. Culoma, D. Wernham, and W. Veith, 2008: Characterization and qualification status of the ADM-Aeolus mission. *Proc. 24th Int. Laser Radar Conf.,* Boulder, CO, International Radiation Commission, 41–44.

ESA, 1999: The four candidate Earth Explorer core missions: 4. Atmospheric Dynamics Mission. ESA SP-1233(4), 157 pp.

——, 2008: ADM-Aeolus Science Report, ESA Rep. SP-1311, 121 pp.

Fiedler, J., G. Baumgarten, and G. von Cossart, 2008: A middle atmosphere lidar for multi-parameter measurements at a remote site. *Proc. 24th Int. Laser Radar Conf.,* Boulder, CO, International Radiation Commission, 824–827.

Fischer, K. W., V. J. Abreu, W. R. Skinner, J. E. Barnes, M. J. McGill, and T. D. Irgang, 1995: Visible wavelength Doppler lidar for measurement of wind and aerosol profiles during day and night. *Opt. Eng.,* **34,** 499–511.

Flamant, P. H., J. Cuesta, M. L. Denneulin, A. Dabas, and D. Huber, 2008: ADM-Aeolus retrieval algorithms for aerosol and cloud products. *Tellus,* **60A,** 273–286.

Flesia, C., and C. L. Korb, 1999: Theory of the double-edge molecular technique for Doppler lidar wind measurement. *Appl. Opt.,* **38,** 432–440.

——, ——, and C. Hirt, 2000: Double-edge molecular measurement of lidar wind profiles at 355 nm. *Opt. Lett.,* **25,** 1466–1468.

Garnier, A., and M. L. Chanin, 1992: Description of a Doppler Rayleigh LIDAR for measuring winds in the middle atmosphere. *Appl. Phys.,* **55B,** 35–40.

Gentry, B. M., H. Chen, and S. X. Li, 2000: Wind measurements with 355-nm molecular Doppler lidar. *Opt. Lett.,* **25,** 1231–1233.

——, and Coauthors, 2008: New technologies for direct detection Doppler lidar: Status of the TWiLiTE airborne molecular Doppler lidar project. *Proc. 24th Int. Laser Radar Conf.,* Boulder, CO, International Radiation Commission, 239–243.

Grund, C., and E. Eloranta, 1991: Fiber-optic scrambler reduces the bandpass range dependence of Fabry-Perot étalons used for spectral analysis of lidar backscatter. *Appl. Opt.,* **30,** 2668–2670.

Hovis, F. E., J. Edelman, T. Schum, J. Rudd, and K. Andes, 2008: Single frequency lasers for high altitude aircraft applications. *Proc. 24th Int. Laser Radar Conf.,* Boulder, CO, International Radiation Commission, 3–6.

Huang, W., and Coauthors, 2009: Field demonstration of simultaneous wind and temperature measurements from 5 to 50 km with a Na double-edge magneto-optic filter in a multi-frequency Doppler lidar. *Opt. Lett.,* **34,** 1552–1554.

Huffaker, R. M. Ed., 1978: Feasibility study of satellite-borne lidar global wind monitoring system. NOAA Tech. Memo. ERL WPL-37, 276 pp.

——, T. R. Lawrence, M. J. Post, J. T. Priestley, F. F. Hall, R. A. Richter, and R. J. Keeler, 1984: Feasibility studies for a global wind measuring satellite system (Windsat): Analysis of simulated performance. *Appl. Opt.,* **23,** 2523–2536.

Imaki, M., and T. Kobayashi, 2005: Ultraviolet high-spectral-resolution Doppler lidar for measuring wind field and aerosol optical properties. *Appl. Opt.,* **44,** 6023–6030.

Irgang, T. D., P. B. Hays, and W. R. Skinner, 2002: Two-channel direct detection Doppler lidar employing a charge-coupled device as a detector. *Appl. Opt.,* **41,** 1145–1155.

ISO, 1999: Lasers and laser-related equipment—Test methods for laser beam parameters. International Organization for Standardization Rep. 11146, 26 pp.

Köpp, F., S. Rahm, and I. Smalikho, 2004: Characterization of aircraft wake vortices by 2-μm pulsed Doppler lidar. *J. Atmos. Oceanic Technol.,* **21,** 194–206.

Korb, C. L., B. M. Gentry, and C. Weng, 1992: The edge technique: Theory and application to the lidar measurement of atmospheric winds. *Appl. Opt.,* **31,** 4202–4213.

——, ——, and S. X. Li, 1997: Edge technique Doppler lidar wind measurements with high vertical resolution. *Appl. Opt.,* **36,** 5976–5983.

——, ——, ——, and C. Flesia, 1998: Theory of the double-edge technique for Doppler lidar wind measurment. *Appl. Opt.,* **37,** 3097–3104.

Leike, I., J. Streicher, C. Werner, V. Banakh, I. Smalikho, W. Wergen, and A. Cress, 2001: Virtual Doppler lidar instrument. *J. Atmos. Oceanic Technol.,* **18,** 1447–1456.

Li, Z., C. Lemmerz, U. Paffrath, O. Reitebuch, and B. Witschas, 2010: Airborne Doppler lidar investigation of the sea surface reflectance at the ultraviolet wavelength of 355 nm. *J. Atmos. Oceanic Technol.,* in press.

Liu, Z., and T. Kobayashi, 1996: Differential discrimination technique for incoherent Doppler lidar to measure atmospheric wind and backscatter ratio. *Opt. Rev.,* **3,** 47–52.

——, W. B. Chen, T. L. Zhang, J. W. Hair, and C. Y. She, 1997: An incoherent Doppler lidar for ground-based atmospheric wind profiling. *Appl. Phys.,* **64B,** 561–566.

——, B. Y. Liu, Z. G. Li, Z. A. Yan, S. H. Wu, and Z. B. Sun, 2007: Wind measurements with incoherent Doppler lidar based on iodine filters at night and day. *Appl. Phys.,* **88B,** 327–335.

——, ——, S. H. Wu, Z. G. Li, and Z. J. Wang, 2008: High spatial and temporal resolution mobile incoherent Doppler lidar for sea surface wind measurements. *Opt. Lett.,* **33,** 1485–1487.

Marseille, G. J., and A. Stoffelen, 2003: Simulation of wind profiles from a space-borne Doppler wind lidar. *Quart. J. Roy. Meteor. Soc.,* **129,** 3079–3098.

McGill, M. J., and J. D. Spinhirne, 1998: Comparison of two direct detection Doppler lidar techniques. *Opt. Eng.,* **37,** 2675–2686.

——, W. R. Skinner, and T. D. Irgang, 1997a: Analysis techniques for the recovery of winds and backscatter coefficients from a multiple-channel incoherent Doppler lidar. *Appl. Opt.,* **36,** 1253–1268.

——, ——, and ——, 1997b: Validation of wind profiles measured with incoherent Doppler lidar. *Appl. Opt.,* **36,** 1928–1939.

McKay, J. A., 1998a: Modeling of direct detection Doppler wind lidar. I. The edge technique. *Appl. Opt.,* **37,** 6480–6486.

——, 1998b: Modeling of direct detection Doppler wind lidar. II. The fringe imaging technique. *Appl. Opt.,* **37,** 6487–6493.

——, 2002: Assessment of a multibeam Fizeau wedge interferometer for Doppler wind lidar. *Appl. Opt.,* **41,** 6487–6493.

Morancais, D., F. Fabre, M. Schillinger, J.-C. Barthes, M. Endemann, and A. Culoma, 2004: ALADIN: The first European lidar in space. *Proc. 22nd Int. Laser Radar Conf.,* Matera, Italy, International Radiation Commission, 127–129.

Nardell, C. A., P. B. Hays, J. Pavlich, M. Dehring, and G. Sypitkowski, 2002: GroundWinds New Hampshire and the LIDARFest 2000 campaign. *Remote Sensing for Industry and Environment Monitoring II,* U. N. Singh, Ed., International Society for Optical Engineering (SPIE Proceedings, Vol. 4484), 36–50.

Paffrath, U., 2006: Performance assessment of the Aeolus Doppler wind lidar prototype. Ph. D. dissertation, Technische Universität München and DLR Forschungsbericht, 137 pp.

——, C. Lemmerz, O. Reitebuch, B. Witschas, I. Nikolaus, and V. Freudenthaler, 2009: The airborne demonstrator for the direct-detection Doppler wind lidar ALADIN on ADM-Aeolus. Part II: Simulations and Rayleigh receiver radiometric performance. *J. Atmos. Oceanic Technol.,* **26,** 2516–2530.

Reitebuch, O., C. Werner, I. Leike, P. Delville, P. H. Flamant, A. Cress, and D. Engelbart, 2001: Experimental validation of wind profiling performed by the airborne 10-μm heterodyne Doppler lidar WIND. *J. Atmos. Oceanic Technol.,* **18,** 1331–1344.

——, E. Chinal, Y. Durand, M. Endemann, R. Meynart, D. Morancais, and U. Paffrath, 2004: Development of an airborne demonstrator for ADM-Aeolus and campaign activities. *Proc. 22nd Int. Laser Radar Conf.,* Matera, Italy, International Radiation Commission, 1007–1010.

——, U. Paffrath, D. Huber, and I. Leike, 2006: ADM-Aeolus level 1B products. ESA Rep. AE-RP-DLR-L1B-001, 62 pp. [Available online at http://eopi.esa.int/esa/esa?cmd=aodetail&aoname=AeolusCalVal.]

——, and Coauthors, 2008: Pre-launch validation of ADM-Aeolus with an airborne direct-detection wind lidar. *Proc. 24th Int. Laser Radar Conf.,* Boulder, CO, 41–44.

Schillinger, M., D. Morancais, F. Fabre, and A. J. Culoma, 2003: ALADIN: The LIDAR instrument for the AEOLUS mission. *Sensors, Systems, and Next-Generation Satellites VI,* H. Fujisada et al., Eds., International Society for Optical Engineering (SPIE Proceedings, Vol. 4881), 40–51.

Schmitt, N. P., W. Rehm, T. Pistner, P. Zeller, H. Diehl, and P. Navé, 2007: The AWIATOR airborne LIDAR turbulence sensor. *Aerosp. Sci. Technol.,* **11,** 546–552.

Schröder, T., C. Lemmerz, O. Reitebuch, M. Wirth, C. Wührer, and R. Treichel, 2007: Frequency jitter and spectral width of an injection-seeded Q-switched Nd:YAG laser for a Doppler wind lidar. *Appl. Phys.,* **87B,** 437–444.

She, C.-Y., J. Yue, Z.-A. Yan, J. W. Hair, J.-J. Guo, S.-H. Wu, and Z.-S. Liu, 2007: Direct-detecion Doppler wind measurement with a Cabannes-Mie lidar: A. Comparison between iodine vapor filter and Fabry-Perot interferometer methods. *Appl. Opt.,* **46,** 4434–4443.

Shen, F., H. Cha, D. Sun, D. Kim, and S. O. Kwon, 2008: Low tropospheric wind measurement with Mie Doppler lidar. *Opt. Rev.,* **15,** 204–209.

Souprayen, C., A. Garnier, A. Hertzog, A. Hauchecorne, and J. Porteneuve, 1999: Rayleigh-Mie Doppler wind lidar for atmospheric measurements. I. Instrumental setup, validation, and first climatological results. *Appl. Opt.,* **38,** 2410–2421.

Stoffelen, A., and Coauthors, 2005: The Atmospheric Dynamics Mission for global wind field measurement. *Bull. Amer. Meteor. Soc.,* **86,** 73–87.

Sun, D., F. Shen, H. Cha, D. Zhang, and J. Dong, 2008: Development of commercial wind lidar receiver. *Proc. 24th Int. Laser Radar Conf.,* Boulder, CO, International Radiation Commission, 284–286.

Tan, D. G. H., and Coauthors, 2008: The ADM-Aeolus wind retrieval algorithms. *Tellus,* **60A,** 191–205.

Tenti, G., C. D. Boley, and R. C. Desai, 1974: On the kinetic model description of Rayleigh-Brillouin scattering from molecular gases. *Can. J. Phys.,* **52,** 285–290.

Weissmann, M., R. Busen, A. Dörnbrack, S. Rahm, and O. Reitebuch, 2005: Targeted observations with an airborne wind lidar. *J. Atmos. Oceanic Technol.,* **22,** 1706–1719.

Werner, C., and Coauthors, 2001: Wind infrared Doppler lidar instrument. *Opt. Eng.,* **40,** 115–125.

Wirth, M., A. Fix, P. Mahnke, H. Schwarzer, F. Schrandt, and G. Ehret, 2009: The airborne multi-wavelength water vapor differential absorption lidar WALES: System design and performance. *Appl. Phys.,* **96B,** 201–213.

Witschas, B., 2007: Characterisation of beam profile and frequency stability of an injection-seeded Nd:YAG laser for a Doppler wind lidar system. M.S. thesis, Department of Technical Physics, University of Applied Sciences Munich, 102 pp.

Xia, H., D. Sun, Y. Yang, F. Shen, J. Dong, and T. Kobayashi, 2007: Fabry-Perot interferometer based Mie Doppler lidar for low tropospheric wind observation. *Appl. Opt.,* **46,** 7120–7130.

Yoe, J. G., and Coauthors, 2003: GroundWinds 2000 field campaign: demonstration of new Doppler lidar technology and wind lidar data intercomparison. *Proc. SPIE Lidar Remote Sensing for Industry and Environment Monitoring III,* **4893**, Hangzhou, China, 327–336.